

High-order disclinations in space-variant polarization

B Khajavi^{1,2} and E J Galvez¹

¹Department of Physics and Astronomy, Colgate University, Hamilton, NY, USA

²Department of Physics and Astronomy, Florida Atlantic University, Boca Raton, FL, USA

E-mail: egalvez@colgate.edu

Received 3 April 2016, revised 23 May 2016

Accepted for publication 10 June 2016

Published 7 July 2016



Abstract

We present the investigation of high-order disclination patterns in the spatially variable polarization of a light beam. The beam was prepared by encoding two distinct high-order optical vortices on each of the circular polarization components of the beam. As a consequence, we were able to produce high-index lemon and star patterns, which have positive and negative indices, respectively. By varying the asymmetry of one of the vortices we were able to transform one symmetric pattern (lemon or star) into another (lemon or star). With one exception, monstar patterns always appear for specific ranges of asymmetry regardless of the end symmetric patterns. Mapping of all disclinations within each case is contained in a spherical space, where monstar regions are cusp-shaped. We found that high-order monstar patterns can have positive or negative index.

Keywords: polarization singularities, C-points, monstars, disclinations

(Some figures may appear in colour only in the online journal)

1. Introduction

Recent developments in the encoding of spatial modes onto light beams have allowed the generation of optical beams with spatially variable polarization. The latter is the result of non-separable superpositions of spatial mode and polarization [1]. The polarization patterns that these beams carry contain disclinations, or rotational dislocations in directional order. The singular point in the dislocation is also known as the C-point [2]. Experimentally, these beams can be produced either by superposition [1, 3–9]; or by passage through optical elements: spatially variable birefringent plates [10], liquid-crystals with spatially variable birefringence [11–13], optical elements with stress birefringence [14], optical fibers [15–17], or subwavelength gratings [18]. These beams are increasingly finding applications in classical communications [19] and in quantum information [20]. These methods also allow a greater exploration of disclinations, by preparing them deliberately.

Lowest-order polarization disclinations are classified as lemons, stars and monstars [2, 21–23]. They are characterized by their index I_C , denoting the rotation of the disclination per circulation around the singularity. They have been studied

widely in speckle fields produced by nonlinear [24, 25] and inhomogeneous media [26, 27], but not until recently have monstars, purely asymmetric patterns, been realized in the laboratory using designer optical beams [6, 7]. Most of these demonstrations have involved first-order singularities: $I_C = \pm 1/2$, or half-turn per circulation about the singularity. By extension, they also occur with high disclination indices. Some higher-order patterns, have been investigated in the context of vector beams [11, 28], but the systematic investigation of higher indices has been limited to theory [29–31].

In this work we present a study of the generation of beams with space-variant polarization encoding disclination patterns of high index, both symmetric and asymmetric. We do this by exploring the superpositions of two modes carrying azimuthal phase, such as Laguerre–Gauss (LG), in orthogonal states of circular polarization. In this work we do not image the far-field modes, so suffices to say that we prepare modes carrying phase dislocations, or optical vortices. Thus, this work may not be limited to LG modes, and so could include other modes, such as Bessel modes. By varying the asymmetry of one of the phase dislocations we are able to generate

new asymmetric patterns not seen before. Some of our findings are surprising, as shown below.

2. Basic definitions

Because we work with light in free space at low powers, we can assume linear behavior throughout. We use non-separable superpositions of spatial modes and polarization to investigate polarization disclination patterns and optical singularities. Space-variant polarization patterns appear when the spatial-mode function and polarization of the mode cannot be separated.

2.1. Superposition of polarization and spatial states

We prepare and image a light mode with two orthogonal circularly polarized components each carrying a distinct optical vortex. This mode is described by

$$U(r, \phi) = f(r)[(\cos \beta e^{i\ell_1 \phi} + \sin \beta e^{-i\ell_1 \phi} e^{i\gamma}) \hat{e}_R + e^{i\ell_2 \phi} e^{i\delta} \hat{e}_L], \quad (1)$$

where β , γ and δ are phases, and r and ϕ are the polar coordinates in the plane perpendicular to the propagation direction. ℓ_1 and ℓ_2 are the topological charges of the spatial modes with radial variation $f(r)$, and \hat{e}_R and \hat{e}_L denote right and left circularly polarized states, respectively. Without any loss of generality we will set $\ell_1 > 0$. We note that in the far field, modes with distinct topological charge have amplitudes with distinct radial dependence, but in our work we re-image the light to the near field: an input fundamental Gaussian mode with distinct phase encodings in the polarization components. Thus, in our image plane

$$f(r) = e^{-r^2/w^2}, \quad (2)$$

where w is the half width of the beam. This method of imaging is not limiting at all, because in the far field, the radial dependencies of the modes with distinct topological charges only affect the ellipticity of the space-variant polarization, leaving the orientation disclinations unchanged.

The spatial mode with right-circular polarization in equation (1) has two phase vortices of the same absolute value but opposite sign. We have considered previously the case of two phase vortices of distinct absolute value and sign, and imaged them in the far field [8]. This gives rise to a pattern of composite C-points that consists of several disclinations in the same beam. The use of two vortices of the same magnitude but opposite sign, as described in equation (1), allows us to study only one central disclination pattern but with a much greater control over its degree of asymmetry.

2.2. Disclination patterns

Space variant polarization patterns are a consequence of non-separable superpositions of spatial mode and polarization. When the spatial modes involve optical vortices, these patterns encode disclinations in the orientation of the

polarization ellipse. That is, the disclination lines, or dislocations in the rotational order, are formed by the directions of the semi-major axes of the polarization ellipses of the vector field.

The index of the lines in a disclination is defined as the number of turns that the orientation θ of the lines makes per turn around the singularity or C-point [23]:

$$I_C = \frac{1}{2\pi} \int d\theta. \quad (3)$$

Because of the circular symmetry, it is useful to define the radial orientation, or the orientation relative to the radial direction:

$$\theta_r = \theta - \phi. \quad (4)$$

Disclination patterns are characterized by radial lines, which are purely radial disclination lines (i.e., with $\theta_r = n\pi$, with n integer). For lemons and stars the radial orientation changes by half a turn in between radial lines. In general, disclination patterns contain one or more angular sectors separated by radial lines. Because of the cyclic nature of the angular variables, the number of radial lines N is equal to the number of sectors. Thus

$$N = \frac{1}{\pi} \left| \int d\theta_r \right|. \quad (5)$$

The absolute value is for keeping N as a countable variable. Replacing equation (4) into (5) and using the definition of equation (3), we get

$$N = |2(I_C - 1)|. \quad (6)$$

The exception to equation (6) is the case with $I_C = +1$ because the orientation varies at the same rate as the angular variable. We will devote to this case separately below.

Consider the cases $\beta = 0^\circ$ and $\beta = 90^\circ$ in equation (1). The orientation of the semi-major axis of the polarization ellipse is half of the relative phase between the two polarization components. Because this phase varies linearly with ϕ , the orientation is

$$\theta = \frac{1}{2}(\Delta\ell\phi - \delta'), \quad (7)$$

where $\Delta\ell = \ell_1 - \ell_2$ and $\delta' = \delta$ for $\beta = 0^\circ$; but $\Delta\ell = -\ell_1 - \ell_2$ and $\delta' = \delta - \gamma$ for $\beta = 90^\circ$. The orientation is not a function of the radial coordinate r . Applying equations (3) and (6) to these two cases yields

$$I_C = \frac{\Delta\ell}{2} \quad (8)$$

and

$$N = |\Delta\ell - 2|. \quad (9)$$

Because monstars have been defined and studied only for lowest-order disclinations, we need to extend their definition for high orders: hyperlemons or hyperstars, symmetric or asymmetric, have a number of radial lines given by equation (6), whereas monstars do not. We expand on this below. Equations (6) and (9) have been derived before in the general context of non-collinear superpositions [31]. That study included high-order symmetric disclinations and

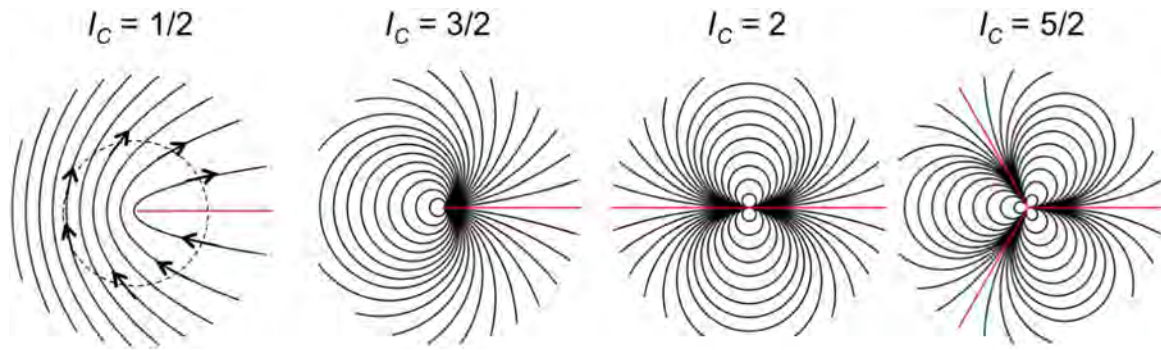


Figure 1. Symmetric disclination patterns with positive index I_C correspond to lemons and hyperlemons. They are created by superpositions of topological charges (ℓ_1, ℓ_2) and $\beta = 0$ in equation (1). The cases shown correspond to $I_C = 1/2$ with $(1, 0)$; $I_C = 3/2$ with $(2, -1)$; $I_C = 2$ with $(3, -1)$; and $I_C = 5/2$ with $(1, -4)$. Red solid lines denote radial lines. The case for $I_C = 1/2$ has arrows added to illustrate the rotation of the orientation of the line around the singularity.

asymmetric cases caused by the non-collinearity of the superposition.

3. C-point characterizations

Here we consider the particular cases of equation (1) that give rise to high-order singularities. We will first present the cases of symmetric lemons and stars, and continue into the asymmetric case of monstars.

3.1. Lemons and hyperlemons

These types of patterns occur for $I_C > 0$. The case with the smallest index, $I_C = 1/2$, can be produced by making $\ell_1 = 1$ and $\ell_2 = 0$. When $\beta = 0$ in equation (1), the pattern with this choice of ℓ_1 and ℓ_2 is produced by a mode with a symmetric phase vortex with right circular polarization superimposed with a mode of constant phase with left circular polarization. This gives rise to a C-point pattern that is symmetric. That is, the rate of change of the orientation is constant: $1/2$ per equation (7). This is a case when the ellipse rotates by half a turn when following a closed path around the C-point. For this case $N = 1$.

This rotation along a closed path is illustrated by arrows in corresponding left-most pattern shown in figure 1. We note that the arrows do not represent the field; they are meant only to illustrate the correlation between the pattern and the index I_C (i.e., the rotation of the orientation of semi-major axis of the polarization ellipse around the singularity). The phase of the electric field within the polarization ellipse also advances with ϕ as we travel along the path. This phase, also known as the rectifying phase, is given by one half the sum of the phases of the right and left circular components [22]. In the case shown, the field advances by π after the round trip along the closed path so that even as the polarization plane rotated by half a turn, the field advances so that it returns to the starting point of the path with the same amplitude and direction with which it started.

Lemons with singularity index higher than $1/2$ are also known as hyperlemons [29]. In figure 1 we show the line patterns of hyperlemons of increasing index. For lemons with

$I_C > 1/2$, the main characteristic is the pattern of closed curves that begin and end at the center of the pattern, also referred to as flower petals [29]. The number of petals is numerically the same as the number of radial lines (colored red in the figure). Hyperlemons can have more than one radial line. The line structure for a given value of I_C is the same for combinations of vortices that have the same value of $\Delta\ell$. For example, $\Delta\ell = 3$ gives rise to the pattern for $I_C = +3/2$, which can be implemented for $\beta = 0$ by values of (ℓ_1, ℓ_2) given by $(2, -1)$, $(3, 0)$ and $(4, 1)$. The disclination patterns for these cases are the same in the near-field as in the far field. However, the ellipticity of the patterns in the far field is not the same for distinct values of (ℓ_1, ℓ_2) . This is because diffraction reshapes the amplitude of the modes according to the value of the topological charge, yielding ellipticities with distinct radial dependencies [8].

3.2. Stars and hyperstars

Stars occur for $I_C < 0$. Consider the case $I_C = -1/2$, implemented by setting $\ell_1 = 1, \ell_2 = 0$ and $\beta = 90^\circ$. This case corresponds to the lowest-order star, which has 3 radial lines. Similar to lemons, stars with index $I_C < -1/2$ are also known as hyperstars. Figure 2 shows examples of hyperstars with increasing values of $|I_C|$. Stars are characterized by the number of points, which is the same as the number of radial lines. They have also been referred to as ‘spider webs’ [29]. For the case $I_C = -1/2$ we display arrows to illustrate the rotation of the lines around the singularity. Note also that from radial line to radial line the radial orientation changes by half a turn. This is true also for the patterns of figure 1.

For stars, the number of radial lines increases with the magnitude of I_C . The angular orientation of the symmetric cases of lemon and star patterns can be varied by changing δ for $\beta = 0$, and δ and γ for $\beta = 90^\circ$.

3.3. Monstars and hypermonstars

Up to now, monstars have been studied only for the lowest-index case, $|I_C| = 1/2$. For this case, monstars have $I_C = +1/2$, same as the lemon, but with three radial lines, as the star with $I_C = -1/2$ [21]. This type of singularity is

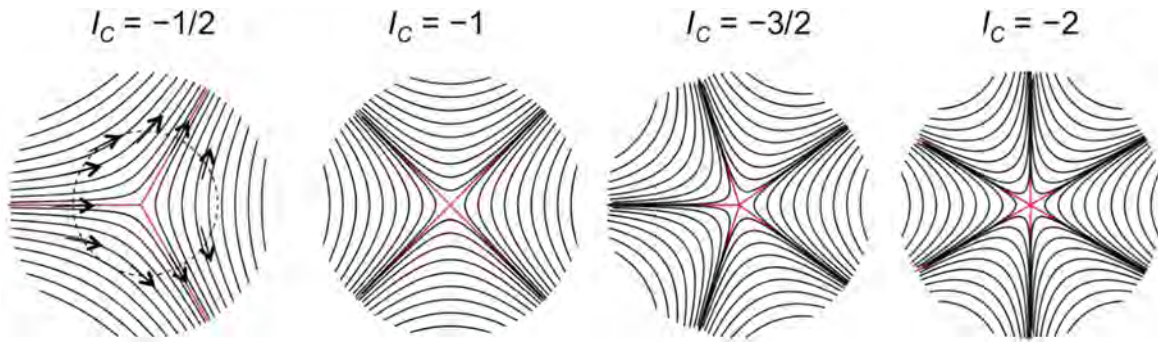


Figure 2. Symmetric disclination patterns with negative index I_C correspond to stars and hyperstars. They are created by superpositions of topological charges (ℓ_1, ℓ_2) and $\beta = 90^\circ$ in equation (1). The cases shown are: $I_C = -1/2$ with $(1, 0)$; $I_C = -1$ with $(3, -1)$; $I_C = -3/2$ with $(2, 1)$; and $I_C = -2$ with $(4, 0)$. Red solid lines denote radial lines. The case for $I_C = -1/2$ has arrows added to illustrate the rotation of the orientation of the line around the singularity.

called monstar because it has similarities to both lemons and stars. Monstars have unique features of their own, but up to now, the default definition of monstars has been: same index as the lemon and same number of radial lines as the star. However, this definition has to be modified to include high-orders, where monstars can have the same index as stars.

One feature of monstars that distinguishes them from lemons and stars is that they have sectors, delimited by radial lines where disinclination lines radiate from the singularity, but their radial orientation does not rotate by π from one radial line to the other. The monstar for $I_C = +1/2$ has two of these sectors. The addition of these sectors produces additional radial lines. The method for finding hypermonstars is then to look for a disclination pattern where the number of radial lines does not follow equation (6).

If the complex coefficients of the right and left circular states are given by z_R and z_L , respectively, as obtained from equation (1), then the radial-line condition can be specified by

$$(1/2)\arg(z_R/z_L) = \phi - n\pi. \quad (10)$$

Setting

$$\text{Im}[(z_R/z_L)\exp(-2\phi + 2n\pi)] = 0, \quad (11)$$

we get

$$\cos \beta \sin \Psi + \sin \beta \sin \Phi = 0, \quad (12)$$

where

$$\Psi = (\ell_1 - \ell_2 - 2)\phi - \delta + 2n\pi \quad (13)$$

and

$$\Phi = (-\ell_1 - \ell_2 - 2)\phi + \gamma - \delta + 2n\pi. \quad (14)$$

We obtained the type of pattern by solving for ϕ in equation (12). The symmetric cases ($\beta = 0^\circ, 90^\circ$) follow in a straight-forward way, resulting in the radial-line directions

$$\phi_r = \frac{2n\pi - \delta'}{2 - \Delta\ell}. \quad (15)$$

This equation gives the angular values of the radial lines in the patterns of figures 1 and 2. As an example of the solution of an asymmetric pattern ($\beta \neq 0^\circ, 90^\circ$), consider the case $(\ell_1, \ell_2) = (1, 0)$ and with $\delta = 0$. At $\gamma = 0$ there are no monstars, and the lemon transforms directly into a star

through the intermediate pattern at $\beta = 45^\circ$ (more on this below). For other values of γ , monstar patterns appear for a range of values of β : $\beta_\gamma \leq \beta < 45^\circ$. The lowest value of β_γ occurs at $\gamma = 180^\circ$, and the highest value converges to 45° as $\gamma \rightarrow 0^\circ, 360^\circ$. Previous work found $\beta_\gamma = 1/\tan^{-1}(1/3)$ for $\gamma = 180^\circ$ [7], obtained by finding the solutions to equation (12), which gives rise to a cubic equation in $\sin \phi$ [32].

Cases with other values of (ℓ_1, ℓ_2) can easily be solved algebraically for simple values of γ . Equation (12) leads to a polynomial equation in powers of $\sin \phi$ of order $N = \max(N_0, N_{90})$. Discriminants in the solution give minimum or maximum allowed values of β_γ that mark the division between number of radial lines for $\beta = 0^\circ$ and $\beta = 90^\circ$. This division is the boundary between lemon or star, and monstar. Some examples of high-order monstar disclinations are shown in figure 3. In all of these cases the patterns do not follow equation (6). The patterns were calculated by numerically solving the disclination-line trajectories. Frames (a) and (b) of figure 3 show monstars for cases $(2, 1)$ and $(3, 0)$, with indices $+1/2$ and $+3/2$, respectively. Monstars are studied in more details in a forthcoming publication [33], but it is important to point out that the monstar in case (c) of figure 3 has a negative index, and the monstar in case (d) had lemons for both $\beta = 0^\circ$ and $\beta = 90^\circ$.

4. Evolution of disclinations and hypermonstardom

It is desirable to find a space that contains a mapping of all possible disclination patterns. The quest for the space that contains the monstars of lowest index, referred to as ‘monstardom,’ led to two types of spaces: planar [34] and spherical [7]. Our goal is to find the range of parameters that give rise to hypermonstars and to investigate all the possible patterns. Because the patterns are represented by two angles, a spherical representation is most adequate. Thus, here we proceed with finding the spherical space of hypermonstars: hypermonstardom. Our search is based on equation (1), which through the angle β creates a transformation from a disclination created by phase vortices ℓ_1 and ℓ_2 at $\beta = 0$, to one

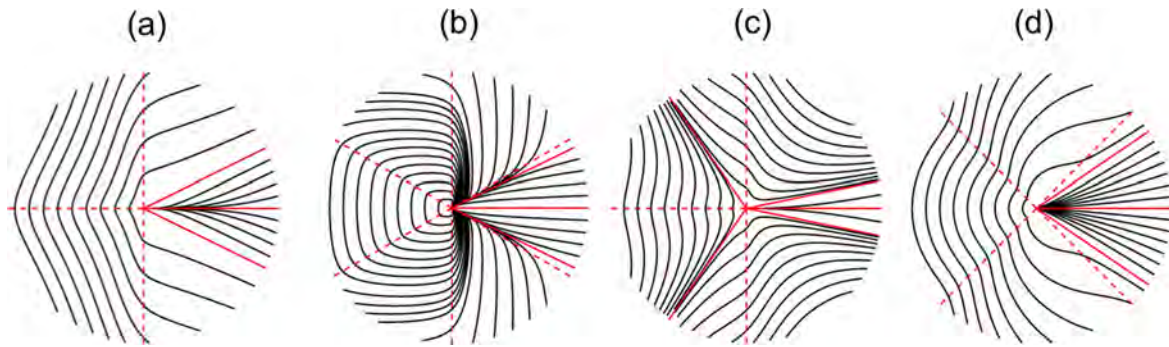


Figure 3. Four examples of monstars: (a) $(\ell_1, \ell_2) = (2, 1)$ for $\beta = 30^\circ$ and $\gamma = 180^\circ$, yielding $I_C = +1/2$; (b) $(3, 0)$ for $\beta = 30^\circ$ and $\gamma = 0^\circ$, yielding $I_C = +3/2$; (c) $(2, 3)$ for $\beta = 30^\circ$ and $\gamma = 180^\circ$, yielding $I_C = -1/2$; and (d) $(2, -3)$ for $\beta = 60^\circ$ and $\gamma = 0^\circ$, yielding $I_C = +1/2$. Solid red lines are radial lines, and dashed red lines correspond to the C-lines of the corresponding cases with $\beta = 45^\circ$. In frames (a) and (c) there are solid and dashed lines superimposed at $\phi = 0$.

with $-\ell_1$ and ℓ_2 at $\beta = 90^\circ$. We will call these ‘end patterns.’ Intermediate values of β give rise to asymmetric disclinations and monstars. The shape and range of disclinations also depend on γ . For $\gamma = 0^\circ, 180^\circ$, the patterns have a mirror symmetry about a horizontal line, as seen in figures 1–3. For the first-order case, δ was found not to give rise to new patterns, but to rotate them [7]. We found this not to be true for $I_C = +1$, but our study of this case is still ongoing. The studies presented here have been largely confined to $\delta = 0$. The pattern with $\beta = 90^\circ$ rotates with γ .

Each of the spaces spanned by the set of values (ℓ_1, ℓ_2) consists of a sphere. Figure 4 gives examples of representative cases. The cases shown represent three distinct situations with respect to the sign of the index of the end patterns: when they are of opposite sign (lemon-star), as for $(3, 0)$; and when they have the same sign: both stars for $(2, 3)$, and both lemon for $(3, -4)$.

For each case of figure 4, we show two perspectives: the first row shows a three-dimensional perspective of the spherical space, and the second row shows a top or bottom view of the sphere above it. For the three cases, the polar angle is 2β and the azimuthal angle is γ . Points on the surface of a sphere map all the distinct disclination patterns for that case. Disclinations within each hemisphere have the same index. The blue and red regions correspond to patterns of the same index as the end patterns. For example, in the first case with $(3, 0)$, the blue and red regions correspond to lemons (with $I_C = +3/2$) and stars (with $I_C = -3/2$), respectively. For $(2, 3)$ blue and red regions correspond to stars of index $I_C = -1/2$ and $I_C = -5/2$, respectively; and similarly, for $(3, -4)$ red and blue regions correspond to lemons of index $I_C = +7/2$ and $I_C = +1/2$, respectively. The yellow regions of all three cases correspond to monstars. Case $(2, 3)$ displays the striking finding that monstars can have negative index. As seen in figure 4, the monstar regions have a peculiar cusp pattern. The number of cusps, distributed evenly about γ must reflect an underlying symmetry that we have not yet determined. Also shown in the figure are sample disclination patterns for each region.

We found that hypermonstars appear in almost every case that we studied. Because of the complexity of most

algebraic solutions of equation (12), we resorted to solving it numerically. We investigated the full range of cases shown in table 1, which correspond to the cases with the lowest indices. The top third of table 1 shows the lemon-star cases, with the first row showing the previously studied case [7, 32]. The table lists the values of ℓ_1 and ℓ_2 , and for each case we list the indices and number of radial lines for the end patterns. As β increases from zero, the pattern transforms from one end pattern to the other, going from the north pole of the sphere to the south pole. As seen in figure 4, this transformation includes a range of values of β for which the patterns are monstars. In the last set of columns we list the index of the monstar, the number of radial lines that it may have, and the extreme value of β_γ that specifies the boundary between the monstar region and either the lemon or star regions. These values correspond to the tip of the cusps in figure 4. Within parenthesis we list the number of cusps that the monstar regions have. Note that there are cases that have the same value of β_γ . For those cases, the corresponding regions of the sphere have identical shapes because the solutions of equation (12) yield the same polynomial equation. The patterns themselves, however, are not the same. The values of β_γ in the tables come from discriminants in the roots of equation (12).

The second and third groups of data in table 1 show the parameters for cases that involved end patterns with index of the same sign. This is the first investigation unveiling this regime of monstars. New findings include the existence of monstars with negative disclination indices, as shown in the second group. This is quite a surprising result because in the first-order cases the monstar index is positive, and without further study, it was thought to be a defining property of monstars. The second and third groups also show results that are corroborated by the spherical spaces of figure 4: the threshold values of β_γ have periodic maxima and minima appearing at symmetric values of γ . For example, the case $(2, 3)$ has three cusps that appear at $\gamma = 60^\circ, 180^\circ, 300^\circ$.

The first two groups of table 1 show a unique finding: the number of radial lines in a monstar disclination can vary within a monstar region. We denote these cases by listing two values for the number of radial lines observed. For example

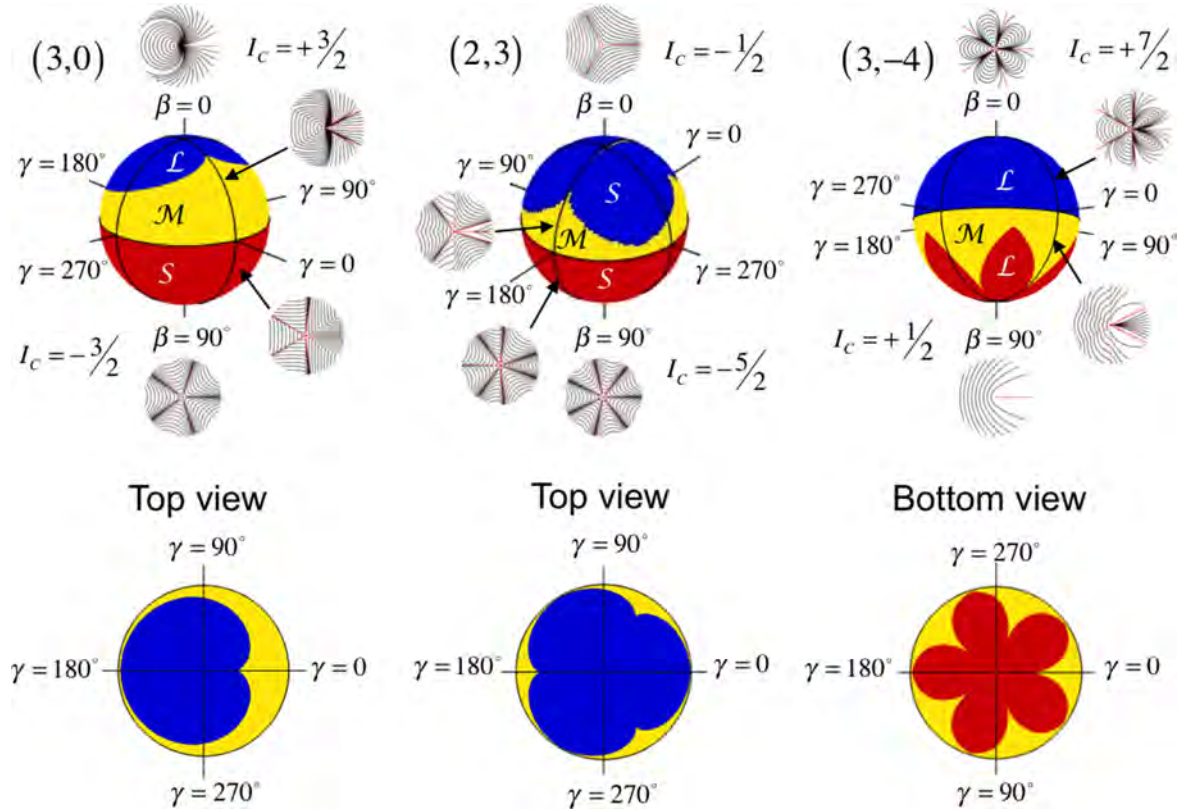


Figure 4. Spherical spaces of high-order disclinations associated with transformations between disclinations of two indices. For each case, the perspective view of the space is shown, and below it, the top or bottom view of the sphere. The cases shown correspond to patterns where the $\beta = 0^\circ$ and $\beta = 90^\circ$ disclinations are respectively lemon with $I_C = +3/2$ and star with $I_C = -3/2$ for $(\ell_1, \ell_2) = (3, 0)$; star with $I_C = -1/2$ and star with $I_C = -5/2$ for $(2, 3)$; and lemon with $I_C = +7/2$ and lemon with $I_C = +1/2$ for $(3, -4)$. Blue and red colors correspond to regions with lemons (L) or stars (S), and yellow correspond to regions with monstars (M). Inserts show examples of disclinations in each region.

Table 1. Characteristics of cases of disclination transformations with the lowest indices.

Case (ℓ_1, ℓ_2)	$\beta = 0^\circ$			$\beta = 90^\circ$			Monstar		
	Pattern	I_C	N	Pattern	I_C	N	I_C	N	β_γ
(1, 0)	Lemon	+1/2	1	Star	-1/2	3	+1/2	3	18.43° (1)
(2, 1)	Lemon	+1/2	1	Star	-3/2	5	+1/2	3, 5	11.31° (1)
(2, -1)	Lemon	+3/2	1	Star	-1/2	3	+3/2	3	18.43° (1)
(3, 0)	Lemon	+3/2	1	Star	-3/2	5	+3/2	3, 5	11.31° (1)
(3, -1)	Lemon	+2	2	Star	-1	4	+2	4	26.57° (1)
(1, 2)	Star	-1/2	3	Star	-3/2	5	-1/2	3	31.0° (3)
(2, 3)	Star	-1/2	3	Star	-5/2	7	-1/2	5,7	23.3° (3)
(1, 3)	Star	-1	4	Star	-2	6	-1	8	33.7° (2)
(1, 4)	Star	-3/2	5	Star	-5/2	7	-3/2	3	35.6° (5)
(1, -2)	Lemon	+3/2	1	Lemon	+1/2	1	—	—	—
(2, -3)	Lemon	+5/2	3	Lemon	+1/2	1	+1/2	3	71.57° (3)
(1, -4)	Lemon	+5/2	3	Lemon	+3/2	1	+3/2	3	71.57° (3)
(3, -4)	Lemon	+7/2	5	Lemon	+1/2	1	+1/2	3	78.69° (5)

Specific cases are labeled by the values of ℓ_1 and ℓ_2 in equation (1). We list the characteristics of the patterns that end at $\beta = 0^\circ$ and $\beta = 90^\circ$, and those of the monstar patterns within the transformations. We list the extreme values of β_γ , and within parentheses the number of cusps in the monstar region.

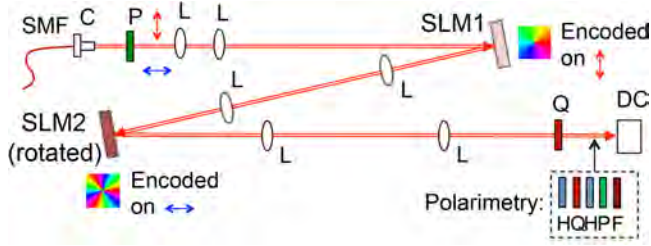


Figure 5. Schematic of the apparatus. Optical elements include lenses (L), half-wave plates (H), quarter-wave plates (Q), polarizer (P), neutral density filter (F), single-mode fiber (SMF), fiber collimator (C), spatial light modulators (SLM), and digital camera (DC). The SLMs were rotated by 90° relative to each other.

the case (2, 1) and $\gamma = 180^\circ$ has a monstar with three radial lines for $\beta \geq 11.43^\circ = \tan^{-1}(1/5)$ and five radial lines for $\gamma = 0^\circ$ and $\beta \geq 38.66^\circ = \tan^{-1}(4/5)$. There was only one case where we did not find monstars: (1, -2). We believe this is so because it is the only case where the end patterns have the same number of radial lines.

5. Experimental setup

The method that we used to investigate the disclinations is similar to one used previously by us [8]. A schematic diagram of the apparatus is shown in figure 5. We used a He-Ne laser beam, with $\lambda = 632.8$ nm, and sent it into a single mode fiber to put the light in a pure Gaussian mode. We then used a collimator and two confocal lenses to expand the beam and fully illuminate the spatial light modulators (SLM). We used a shear interferometer to insure that the wavefront was planar. A polarizer with its axis at about 45° to the horizontal provided the linear (horizontal and vertical) components for independent phase encoding by each SLM. Each SLM applied a phase retardation onto the field component that was parallel to its axis. Therefore, in order to apply two different orthogonal spatial (LG) modes on vertical and horizontal components of the beam, we rotated one of the SLMs.

Collinearity was an important consideration for our experiments, so our apparatus used a same-path interferometer, which guaranteed it, also making the relative phase between the components immune to interferometer instabilities such as vibrations or thermal drifts. Upon reaching the first SLM, one polarization component (vertical) was encoded with the phase of a superposition of topological charges ℓ_1 and $-\ell_1$. The SLM, mounted on an XY stage, was operated in reflection mode. This way, the spatial mode associated with the orthogonal polarization (horizontal) was reflected but not encoded by the SLM, and so it traveled the same path as the vertical component. Past refocusing 4-f optics and a relaying mirror (not shown), the light encountered a second SLM similar to the first one but with its axis rotated by 90° . This SLM encoded in reflection mode a second phase vortex, with topological charge ℓ_2 , onto the horizontal polarization component, leaving the vertical one unaffected.

We used a quarter-wave plate, with fast axis at $\pi/4$ with respect to the horizontal, to put the modal superposition in the circular polarization basis. To best investigate the disclination patterns, we placed another pair of confocal lenses after the second SLM in a 4-f arrangement. The latter re-imaged both SLMs onto a digital camera, providing a near-field or Fresnel view of the original Gaussian mode plus phase/polarization encodings.

In all cases at least one polarization component carried an optical vortex. Thus, in the imaging of the SLMs at the camera there was a small region of radius r_0 of destructive interference. Thus, in practice, equation (1) was satisfied only for $r > r_0$. We also used this spot for alignment purposes. This small region can be seen in all the experimental data shown below. A more detailed analysis of this will be presented elsewhere.

Before the camera we placed a set of polarization filters to perform imaging polarimetry [8, 35]. The images obtained by passage through six polarization filters (horizontal, vertical, diagonal, antidiagonal, right circular and left circular) were used to obtain the Stokes parameters of each imaged point. Because both polarization components had the same (Gaussian) amplitude, the polarization of each imaged point was linear or nearly linear. This defined the orientation well and thus helped the analysis of the disclination patterns.

6. Experimental results

Figures 6–8 show comparisons between the theoretical predictions and experimental measurements for cases (3, 0), (2, 3) and (2, -3), respectively. We have done comparisons for most cases listed in table 1. In all cases the agreement is very good, with the data showing all the disclination features predicted by the theory. Row (1) in the figures shows the calculated disclination patterns. Rows (2) and (3) show respectively the measured and the modeled patterns. The size of each experimental image shown is of about 450 pixels on each side. To better appreciate the disclinations, the state of the polarization was drawn at semi-random locations in the image. We also plot in false color the orientation of the polarization in a useful way: colors encode the orientation relative to the radial direction (θ_r in equation (4)). The color selection is such that yellow specifies the orientation of radial lines and blue specifies the orientation of lines perpendicular to the radial direction. This way it is much easier to identify the radial directions in the data. The cases presented in columns (a) and (c) correspond to the end patterns for $\beta = 0^\circ$ and $\beta = 90^\circ$, respectively. Column (b) shows the pattern corresponding to a monstar.

Case (3, 0) shows patterns not investigated before: a lemon with $I_C = +3/2$, a monstar with $I_C = +3/2$, and a star with $I_C = -3/2$. These patterns have 1, 3 and 5 radial lines, respectively, as seen in Row (1) of the figure 6. The dashed lines represent directions of disclination discontinuities that appear for $\beta = 45^\circ$ [33, 36]. They mark directions of sharp turns in the disclination lines of asymmetric patterns, which get more accentuated the closer β is to

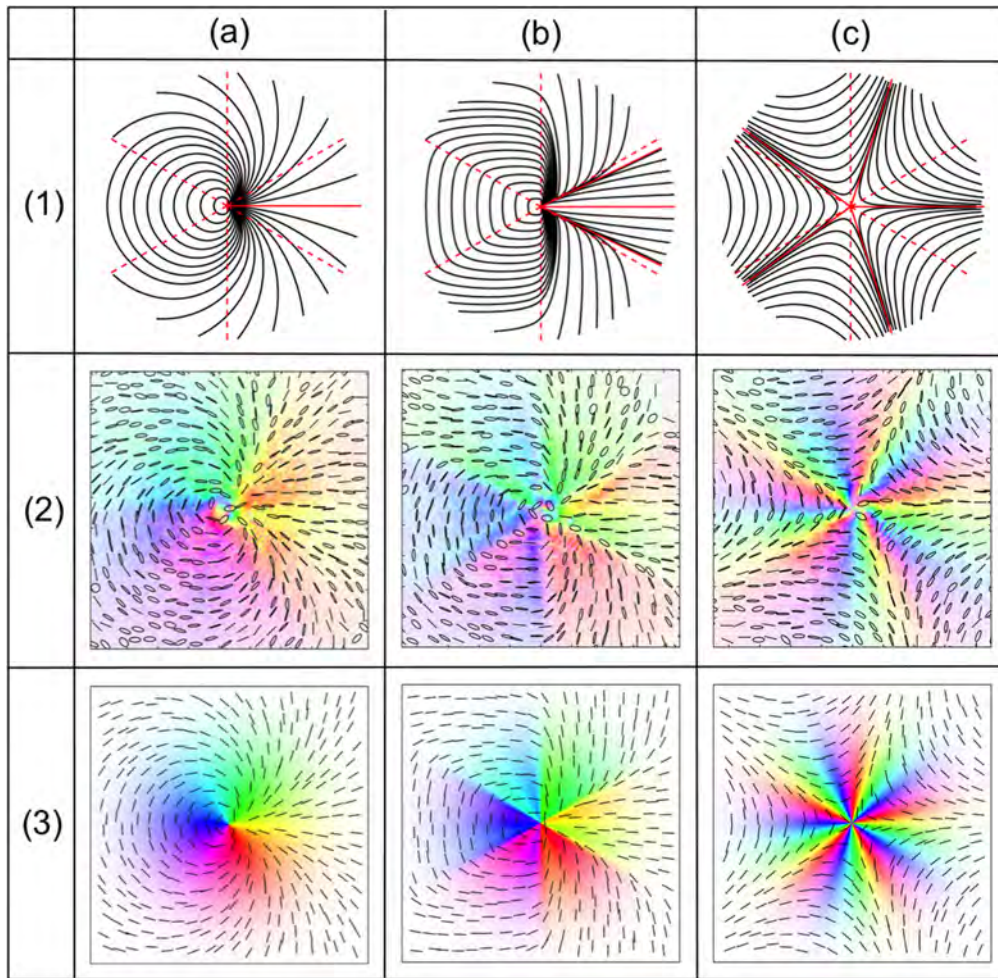


Figure 6. Transformation of a $+1/2$ lemon to a $-3/2$ star through a monstar. All frames correspond to the case $(3, 0)$ with $\gamma = 0^\circ$. They are divided by the value of β : 0° for (a), 30° for (b) and 90° for (c). In the first row red solid lines are radial lines and red dashed lines are C-lines for the $\beta = 45^\circ$ case. The second row is the polarimetry data. The third row is computer generated polarimetry. False color encodes radial orientation, with yellow being the radial direction. Color saturation denotes intensity.

45° . In the far field these lines are C-lines, corresponding to zeros of the mode with right-circular polarization. The main features to notice in the data (row (b)) as it compares to the theoretical modeling (row (c)) are the regions colored yellow. They clearly show the radial lines in the star pattern. The lemon and the monstar have regions of lines where the curvature is very close to radial, and so the yellow coloring is not as sharply defined as in the star pattern. Note that this case refutes what was thought to be one of the features of monstars, present in the lowest-order case, that the monstar has the same number of radial lines as the star. The defining features of monstars are the two sectors bounded by radial lines that contain curved lines radiating from the singularity (i.e. with radial orientation that does not flip between radial lines).

The case $(2, 3)$ of figure 7 represents an important result of this work. It is a case where the monstar has a negative index. The end pattern with $\beta = 0^\circ$ has $I_C = -1/2$ in frame (a). At $\beta = 23.3^\circ$ two radiating-line sectors grow from each of two of the radial lines, producing a monstar pattern with a total of seven radial lines. As β increases, these lines grow into the pattern of figure 3 (b) at $\beta = 43^\circ$. As β becomes $\beta >$

45° four of the radiating sectors merge to become two of the hyperbolic-line sectors of the seven-point star of frame (c), but with two radial lines spontaneously appearing at cusps in the lines when $\beta = 43^\circ$. As $\beta \rightarrow 90^\circ$ the pattern becomes a symmetric seven-point star. In addition to the radiating-line sectors unique to monstars, the pattern has hyperbolic-line sectors that give rise to its negative index. The agreement of the monstar patterns and the modeled ones is remarkable.

The experimental results for $(2, -3)$ and $\gamma = 0$, are shown in figure 8. It is a case where the end patterns are both lemons. All of the monstars that appear in the third group of table 1 have lemon-type sectors plus sectors with radiating lines. Thus, the lemon-type sector in figure 8 generates the positive disinclination index. Note that the undulations in the monstar pattern at the markers of the discontinuities at $\beta = 45^\circ$ (dashed lines in the figure) are seen clearly in the data. We have called these ‘scars’ of the related pattern at $\beta = 45^\circ$ [36]. Small disagreement between the data and modeling, particularly for column (c), is a sign of experimental imperfections rather than a fundamental discrepancy.

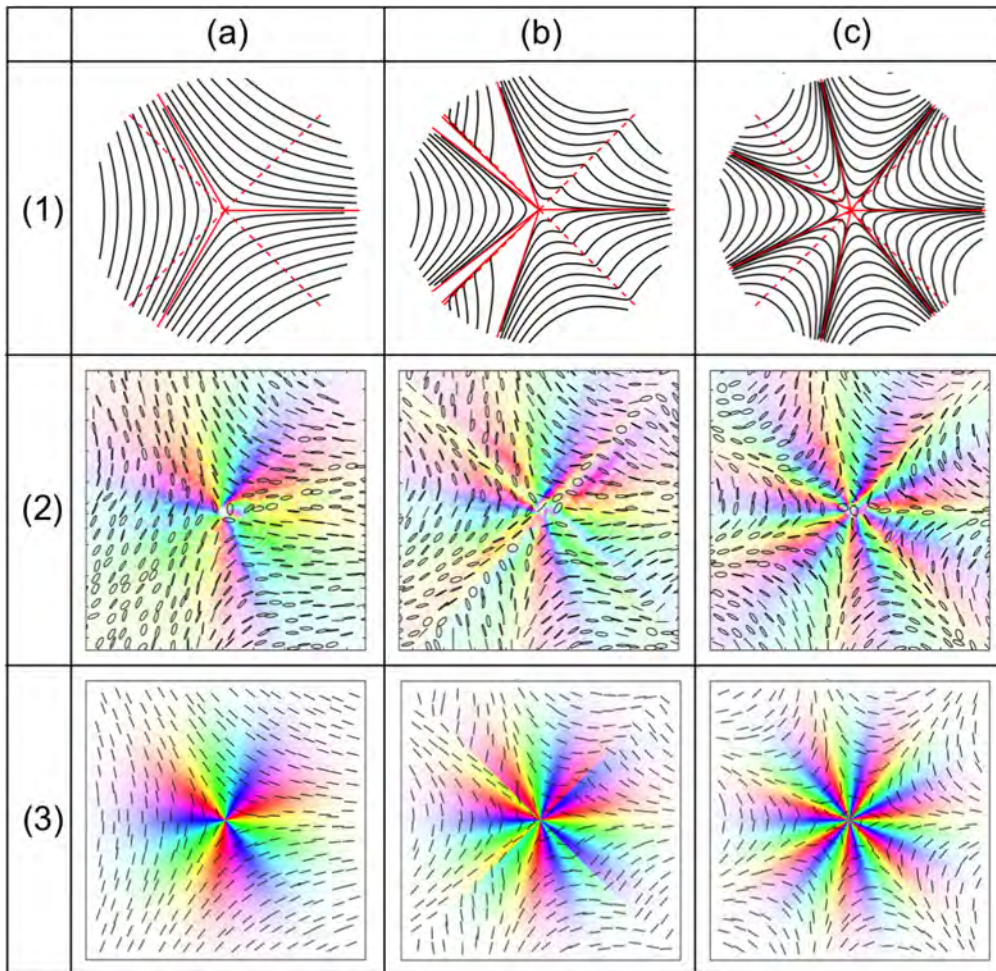


Figure 7. Transformation of a $-1/2$ star to a $-5/2$ star through a monstar. All frames correspond to the case (2, 3) with $\gamma = 0^\circ$. They are divided by the value of β : 0° for (a), 43° for (b) and 90° for (c). In the first row red solid lines are radial lines and red dashed lines are C-lines for the $\beta = 45^\circ$ case. The second row is the polarimetry data. The third row is computer generated polarimetry. False color encodes radial orientation, with yellow being the radial direction. Color saturation denotes intensity.

7. Discussion and conclusions

Polarization patterns around first order singularities have been widely studied in the past, but up to now little was known about higher-order singularities, especially monstars. In this study we investigated high-order asymmetric disclinations, and in particular monstars. Our work was motivated by theoretical calculations of asymmetric disclinations based on the polarization of light. We found new and surprising patterns associated to disclinations with high index. We confirmed our calculations and modelings by direct observations as presented in this article and two others [33, 36]. The overall agreement between measurements and theory is excellent.

From our findings we conclude that monstars appear to be of a general type not previously appreciated. They can have either positive or negative index. Thus, they do not need to have properties of lemons and stars at the same time, as with lowest-order disclinations. They can also have properties of either only. In addition, we recognized that monstars have their own unique feature: sectors delimited by radial lines, with disinclination lines that radiate from the singularity. We

propose that these radiating-line sectors should be the defining characteristic of monstars.

Alternatively, stars and lemons are disclinations that have negative and positive index I_C , respectively, but have disclination lines with specific characteristics. Stars consist of sectors bound by radial lines that contain lines that avoid the singularity in a hyperbolic fashion. Lemons have sectors bound by radial lines that wind about the singularity and, with the exception of $I_C = +1/2$, disinclination lines begin and end at the singularity. In the $I_C = +1/2$ case, the pattern has 1 radial line and its disinclination lines describe parabolic-type trajectories around the singularity. These features are all consequences of the radial orientation of the lines rotating by half a turn between radial lines.

The definitions given above do not include one important case: $I_C = +1$. Is it a lemon or a monstar? This case is exemplified by the radial vector beam. We are investigating further the asymmetric patterns for this case, but already anticipate a main finding [36]: all patterns with this index have more in common with monstars than with lemons. For cases with $\delta \neq \pi$ the disinclination patterns consist of lines

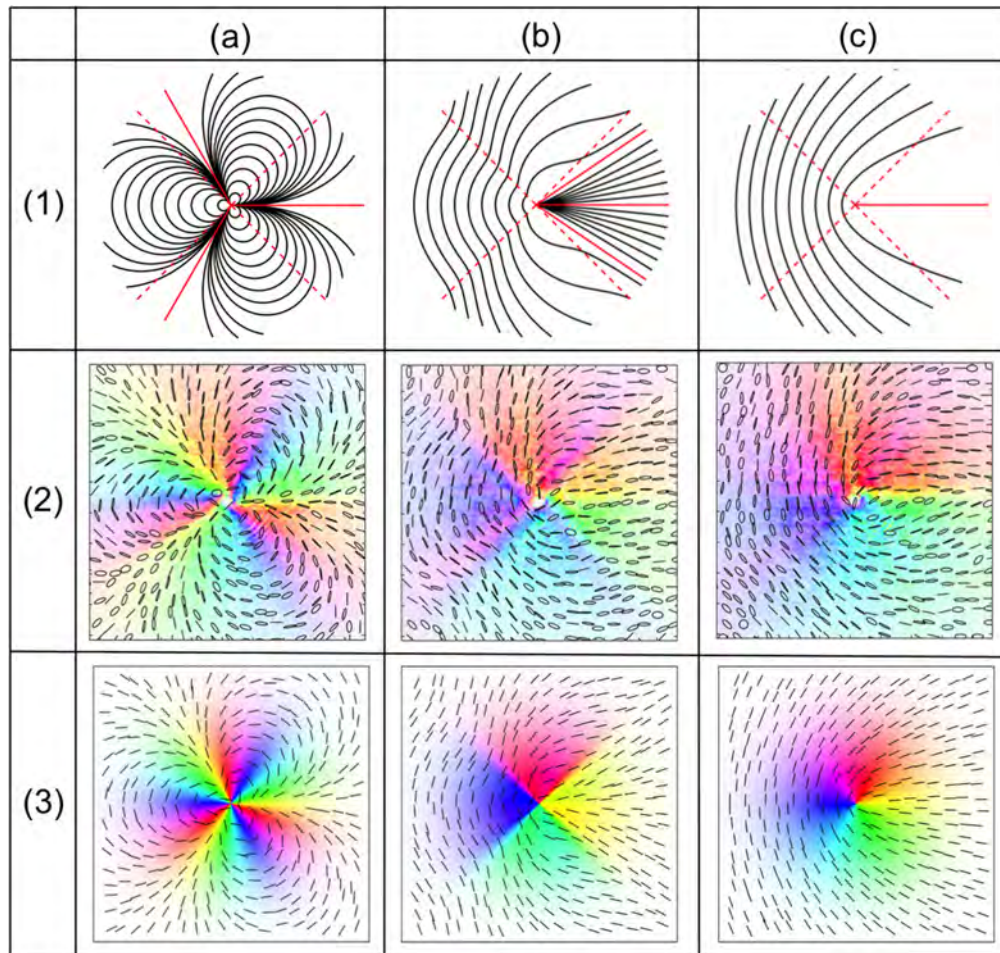


Figure 8. Transformation of a $+1/2$ lemon to a $+5/2$ lemon through a monstar. All frames correspond to the case $(2, -3)$ with $\gamma = 0^\circ$. They are divided by the value of β : 0° for (a), 60° for (b) and 90° for (c). In the first row red solid lines are radial lines and red dashed lines are C-lines for the $\beta = 45^\circ$ case. The second row is the polarimetry data. The third row is computer generated polarimetry. False color encodes radial orientation, with yellow being the radial direction. Color saturation denotes intensity.

that radiate from the singularity. The case $\delta = \pi$ is a unique case, where the disclination lines describe closed curves about the singularity, but do not include it. Thus we are led to conclude, pending further study, that this case belongs more to the monstar classification than to the lemon.

This research on high-order disclinations may inform other physical systems where disclinations are present. It may encourage a more deliberate effort to find these high-order disclinations and study their effects in the properties of the systems in which they belong. Liquid crystals already show interesting interactions with complex light [13, 37]. The study of high-order disclinations in liquid crystals, or their interaction with light bearing high-order disclinations may offer possibilities for new fundamental studies and applications.

Acknowledgments

BK thanks WA Miller for his encouragement. This work was funded by NSF grant PHY-1506321.

References

- [1] Galvez E J, Khadka S, Schubert W H and Nomoto S 2012 *Appl. Opt.* **51** 2925
- [2] Nye J F 1983 *Proc. R. Soc. A* **389** 279
- [3] Zhan Q 2009 *Adv. Opt. Photon.* **1** 1
- [4] Maurer C, Jesacher A, Fürhapter S, Bernet S and Ritsch-Marte M 2007 *New J. Phys.* **9** 78
- [5] Wang X L, Ding J, Ni W J, Guo C S and Wang H 2007 *Opt. Lett.* **32** 3549
- [6] Kumar V, Philip G M and Viswanathan N K 2013 *J. Opt.* **15** 044027
- [7] Galvez E J, Rojec B L, Kumar V and Viswanathan N K 2014 *Phys. Rev. A* **89** 031801
- [8] Khajavi B and Galvez E J 2015 *Opt. Eng.* **54** 111305 1
- [9] Ote E, Schlickriede C, Alpmann C and Denz C 2015 *Proc. SPIE* **9379** 937908
- [10] Dorn R, Quabis S and Leuchs G 2003 *Phys. Rev. Lett.* **91** 233901
- [11] Cardano F, Karimi E, Slussarenko S, Marrucci L, de Lisio C and Santamato E 2012 *Appl. Opt.* **51** C1
- [12] Cardano F, Karimi E, Marrucci L, Lisio C and Santamato E 2013 *Opt. Express* **21** 8815
- [13] Brasselet E 2012 *Phys. Rev. Lett.* **108** 087801
- [14] Beckley A M, Brown T G and Alonso M A 2010 *Opt. Express* **18** 10777

- [15] Volpe G and Petrov D 2004 *Opt. Commun.* **237** 89
- [16] Viswanathan N and Inavalli V 2009 *Opt. Lett.* **34** 1189
- [17] Jayarsuya Y V, Inavalli V V G K and Viswanathan N K 2011 *Appl. Opt.* **50** E131
- [18] Niv A, Biener G, Kleiner V and Hasman E 2005 *Opt. Lett.* **30** 2933
- [19] Milione G *et al* 2015 *Opt. Lett.* **40** 1980
- [20] Nagali E, Sciarrino F, De Martini F, Marrucci L, Piccirillo B, Karimi E and Santamato E 2009 *Phys. Rev. Lett.* **103** 013601
- [21] Berry M V and Hannay J H 1977 *J. Phys. A: Math. Gen.* **10** 1809
- [22] Dennis M R 2002 *Opt. Commun.* **213** 201
- [23] Freund I 2002 *Opt. Commun.* **201** 251
- [24] Flossmann F, Schwarz U T, Maier M and Dennis M R 2005 *Phys. Rev. Lett.* **95** 253901
- [25] Soskin M and Vasil'ev V I 2013 *J. Opt.* **15** 044022
- [26] Soskin M S, Denisenko V and Freund I 2003 *Opt. Lett.* **28** 1473
- [27] Flossmann F, O'Holleran K, Dennis M R and Padgett M J 2008 *Phys. Rev. Lett.* **100** 203902
- [28] Vyas S, Kozawa Y and Apr Sato S 2013 *Opt. Express* **21** 8972
- [29] Freund I 2001 *Opt. Commun.* **199** 47
- [30] Bliokh K Y, Niv A, Kleiner V and Hasman E 2008 *Opt. Express* **16** 695
- [31] Freund I 2011 *Opt. Commun.* **284** 3816
- [32] Galvez E J, Rojec B L and Beach K 2014 *Proc. SPIE* **8999** 89990I
- [33] Galvez E J and Khajavi B in preparation
- [34] Dennis M R 2008 *Opt. Lett.* **33** 2572
- [35] Freund I, Soskin M S and Mokhun A I 2002 *Opt. Commun.* **208** 223
- [36] Galvez E J and Khajavi B 2016 *Proc. SPIE* **9764** 97640R
- [37] Marrucci L, Manzo C and Paparo D 2006 *Phys. Rev. Lett.* **96** 163905